Journal of
Materials Chemistry A

PAPER

View Article Online
View Journal | View Issue

Check for updates

Cite this: *J. Mater. Chem. A*, 2019, **7**, 23973

# Understanding the characteristics of conducting polymer-redox biopolymer supercapacitors†

Musbaudeen O. Bamgbopa,[ab] Jesper Edberg,[c] Isak Engquist,[ab] Magnus Berggren*[ab] and Klas Tybrandt*[ab]

Received 30th June 2019
Accepted 31st July 2019

DOI: 10.1039/c9ta07030c

rsc.li/materials-a

The growth of renewable energy production has sparked a huge demand for cheap and large-scale electrical storage solutions. Organic supercapacitors and batteries are envisioned as one, among several, candidates for this task due to the great abundance of their constituent materials. In particular, the class of supercapacitors based on conjugated polymer-redox biopolymer composites are of great interest, since they combine the benefit of high electrical conductivity of the conducting polymers with the low cost and high specific capacitance of redox biopolymers. The optimization of such complex systems is a grand challenge and until now there have been a lack of models available to ease that task. Here, we present a novel model that combines the charge transport and impedance properties of conducting polymers with the electrochemical characteristics of redox polymers. The model reproduces a wide range of experimental data and elucidates the coupling of several critical processes within these supercapacitors, such as the double-layer capacitance, redox kinetics and dissolution/release of the redox polymer to the electrolyte. Further, the model also predicts the dependencies of the power and energy densities on the electrode composition. The developed model shows how organic supercapacitors can be analyzed beyond archetypical equivalent circuit models and thus constitutes a promising tool for further advancements and optimization within the field of research of green energy storage technology.

## Introduction

The ongoing transition from fossil fuels to renewable energy sources is creating a huge demand for cheap and large-scale electrical energy storage solutions. Organic supercapacitors and batteries have been suggested as a crucial part of the solution, as they are made up of abundant materials that can be processed with low energy consumption.[1,2] Conducting polymers (CPs) have been thoroughly studied for supercapacitors, with reported specific capacitances reaching beyond 500 F $g^{-1}$ for polypyrrole[3] and polyaniline.[4] Unfortunately, these polymers are unstable with a typical degrading performance during cycling, rendering them unsuitable for may applications. PEDOT (poly(3,4-ethylenedioxythiophene)) is currently the most widely used conducting polymers due to its high conductivity, long-term stability, and processability from water dispersions.[5] However, the relatively large monomer size of PEDOT gives a relatively lower specific capacitance, typically reaching the 80–90 F $g^{-1}$ range,[6] which is insufficient for many energy storage applications. Also, the cost of synthesizing and producing CPs, even at large volumes, is still too high for large scale energy storage applications.

One route to partly circumvent the issue of low specific capacitance and high production costs is to amalgamate the CP phase with cheaper redox-active polymers/molecules.[6–8] Here, biopolymers from the forest are certainly of special interest due to their abundance, cheapness and sustainability. By assembling a thin layer of PEDOT:PSS (poly(styrene sulfonate)) onto cellulose nanofibrils (CNF), highly porous and conductive papers can be achieved.[9] Recently, the redox-active polymer lignosulfonate (LS) was incorporated into such paper electrodes, creating supercapacitor positrodes with specific capacitances reaching up to 230 F $g^{-1}$.[10] LS can be directly derived from lignin, being a waste product from wood pulp manufacturing, and represents the 2nd most prevalent biopolymer on earth. This combination of CPs with redox active biopolymers constitutes a highly attractive concept, as it combines the outstanding electrical properties of PEDOT with the high specific capacitance and cheapness of LS. Devices based on this concept generate new challenges from a theoretical and characterization perspective, as both the structural and reaction complexity increase drastically in comparison to pure CP-based supercapacitors. Therefore, careful modelling is necessary to better understand the dynamics and energetics of these devices and to enable further optimization.

---

[a] *Laboratory of Organic Electronics, Department of Science and Technology, Linköping University, 601 74 Norrköping, Sweden. E-mail: klas.tybrandt@liu.se; magnus.berggren@liu.se*

[b] *Wallenberg Wood Science Center, Laboratory of Organic Electronics, Linköping University, 601 74 Norrköping, Sweden*

[c] *RISE Acreo, SE-601 74 Norrköping, Sweden*

† Electronic supplementary information (ESI) available. See DOI: 10.1039/c9ta07030c

A common approach to model supercapacitors is to fit an equivalent circuit model to electrochemical impedance spectroscopy measurements.[11–13] This approach might be adequate for system-level integration of (super)capacitors, but is often insufficient when applied at the device level and more so; such a modelling approach fails in describing the crucial parameters of supercapacitors including redox-active molecules/polymers with complex redox reaction pathways. Such models typically also fail to account for the coupled mass transport of various species within the electrode/electrolyte.

Most early models of CPs were built around the classic Butler–Volmer equations describing them as solely redox electrochemical reactions.[14–16] This approach does not capture the capacitive-like charging behaviour commonly observed in CPs, which sometimes was incorporated as an additional phenomenological term. More recently, models based on the drift-diffusion equations have been developed to properly describe the dynamics of CPs,[17–19] however also these models tend to fail with respect to the volumetric capacitive behaviour,[20] most likely because electrons and ions were assumed to co-exist within the same material phase. Indeed, by explicitly implementing 2D CP nanopores, the capacitive behaviour of CPs can be reproduced qualitatively.[21] To quantitatively reproduce both the dynamics and charging characteristics of CPs, a modified drift-diffusion model was recently developed.[22] By coupling the Fermi level in the semiconductor to the electric double layer residing between the electronic and ionic phases, the full charging and transport characteristics of PEDOT:PSS can be reproduced.[22]

Here, we extend this model to address the complexity of CP redox-enhanced supercapacitors. By coupling the electrochemical redox reactions of LS to the Fermi level of the conducting polymer, the electrode characteristics are reproduced and analysed. When modelling sequences of charging cycles, our model did not only properly describe the charging characteristics, but it also elucidates the interplay between dissolution and mass transport of LS along with its redox reaction kinetics. We apply our developed model to predict the electrode performance of a variety of charge storage device configurations, providing crucial insights in the trade-off between specific power and energy density.

## Experimental

### Numerical simulations

Simulations were executed in COMSOL Multiphysics software version 5.3a; coupling both the *Electrostatics* and *Transport of Species* modules. The models were executed in 1D, where the meshing included finer meshing at the electrode–electrolyte interface and coarser meshing elsewhere. The bulk electrolyte domain has 1000 elements with an element ratio of 0.0001 in an arithmetic sequence distribution, while the electrode mesh has maximums of both element size and growth rate of 1 μm and 1.1, respectively. The galvanostatic charge–discharge cycling was implemented using the *Events* module given cut-off potentials. Modelling operating parameters are included in the ESI.†

### Sample preparation

Lignosulfonic acid sodium salt (MW ∼52 000), glycerol, perchloric acid, and dimethyl sulfoxide (DMSO) was purchased from Sigma Aldrich. PEDOT:PSS (Clevios PH 1000) was purchased from Heraeus. Conductive carbon paste (7102) was purchased from DuPont. Wet proofed Toray carbon paper was purchased from FuelCellStore. All materials were used without further modifications. Cellulose nanofibrils (CNF) were prepared by RISE Bioeconomy. A mixture of water and cellulose fibres were passed 10 times through a microfluidic system at 1700 bars to obtain a suspension of nanofibrils (0.5 wt%). The paper electrodes were prepared by adding 35 mg of lignosulfonate to 2 mL deionised water and stirring using a Vortex mixer until fully dissolved. 4.7 g of PEDOT:PSS solution was then added followed by stirring and sonication for 5 minutes in an ultrasonic bath. 4.42 g of CNF solution, 36 mg glycerol and 258 mg DMSO was subsequently added followed by mixing using a T-10 basic ultra Turrax (IKA) at medium rotation speed for 5 minutes. The mixture was poured into plastic Petri dishes followed by degassing for 1 hour in a vacuum desiccator. The samples were then dried at 60 °C in an oven over night. Reference samples without lignosulfonate were also prepared following the same procedure. The paper samples were cut into circular discs (7 mm diameter) using a hole punching tool and were then subsequently glued onto carbon paper current collectors using carbon paste. The samples were baked on a hotplate for at 60 °C for 15 minutes to dry the paste.

### Characterization

Electrochemical measurements were performed on a potentiostat (SP-200 BioLogic Science Instruments) in a three-electrode setup using a Pt mesh counter electrode, Ag/AgCl reference electrode and 0.1 M $HClO_4$ electrolyte. The choice of electrolyte was based on previous work on PEDOT:LS electrodes.[6,10] Galvanostatic charge–discharge measurements were performed at 1 or 2 A $g^{-1}$ (based on PEDOT + LS mass) between 0–0.7 V.

## Results and discussion

### Electrode system

PEDOT:PSS + CNF + LS electrodes of varying LS content were fabricated and characterized according to the experimental details above (Fig. 1a). The different kinds of electrodes are denoted according to the PEDOT:LS mass ratio, with 1_0 having no LS and 1_2 having 1 : 2 mass ratio. The 1 : 2 mass ratio was chosen based on a previous study,[10] where that ratio produced the highest specific capacitance. Positrodes were characterized in electrolytes containing various concentrations of LS in order to verify the impact of the mass transport of LS between the electrode and the electrolyte on the electrical performance. Fig. 1b gives an overview of the various constituents and processes within the system. As the electrodes initially contain a solid phase of LS, the characteristics of the electrode change over time as the solid LS gradually dissolves into its dissolved form, which then can diffuse within the positrode-electrolyte system. The charging dynamics of the system will include

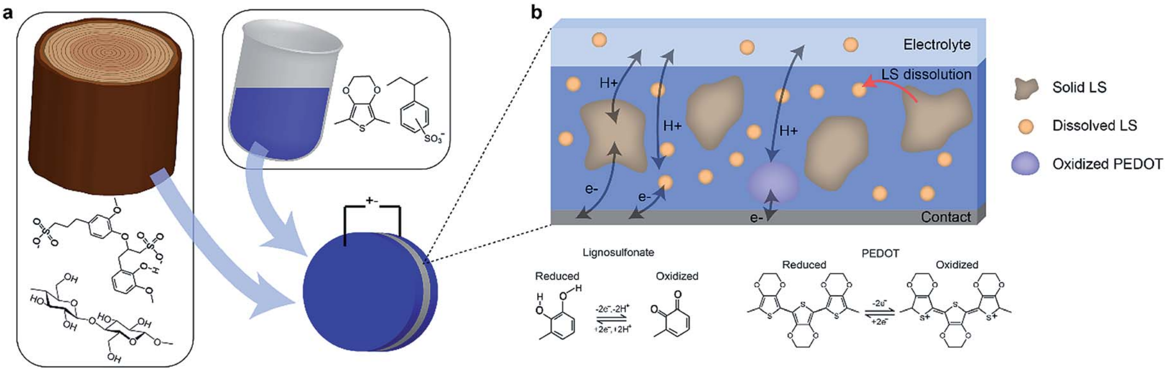

Fig. 1 Paper-based all-organic redox-enhanced supercapacitors. (a) The electrode is made up of nanofibrillated cellulose, PEDOT:PSS and lignosulfonate (LS). (b) Within the electrode, the LS is initially immobilized in its solid form during drying. Once the electrode is in contact with aqueous electrolyte, the solid LS can dissolve. The PEDOT and both solid and dissolved forms of LS participate in the electrode redox reactions.

three contributions; the capacitive charging of the PEDOT and the redox reactions of the solid and dissolved LS.

## Model

To capture the dynamic characteristics of the supercapacitor, the model must account for the coupling between many different quantities and processes, including electrostatic potential, conducting polymer doping level, concentrations of included matter and charged species, mass transport and electrochemical reaction rates. The experimental three-electrode setup is approximated by the 1D model geometry shown in Fig. 2, where the electrode comprises an electronic phase and an ionic phase, while the electrolyte only conducts ions. At galvanostatic test conditions the ensuing boundary conditions are also depicted in Fig. 2.

Within the model, ionic transport is described by the Nernst–Planck–Poisson (NPP) equations throughout the whole system:

$$\frac{\partial c_i}{\partial t} - \nabla\left(D_{c_i}(\nabla c_i + z_i f c_i \nabla V_c)\right) = r_i \tag{1}$$

$$-\frac{\varepsilon \nabla^2 V_c}{F} = p + \sum_i z_i c_i + c_{\text{fix}} \tag{2}$$

where $c_i$ and $D_{c_i}$ are the concentration and diffusivity of the included ionic species respectively, $V_c$ is the electrostatic potential within the ionic phase, $r_i$ is the generation/consumption rate of the respective species, $p$ is the hole concentration in the PEDOT, $c_{\text{fix}}$ is the concentration of fixed charges (*i.e.* $\text{PSS}^-$), and $f = F/RT$. Note that $p$ and $c_{\text{fix}}$ in eqn (2) are non-existent within the external electrolyte (see Fig. 2).

The hole transport within the PEDOT phase is described by modified NPP equations which take into accounts the shift in Fermi level due to the density of states:[22]

$$\frac{\partial p}{\partial t} - \nabla\left(D_p\left(\nabla p + f p \nabla\left(V_p + \mu_p/e\right)\right)\right) = r_p \tag{3}$$

$$-\frac{\varepsilon \nabla^2 V_p}{F} = p - \left(V_p - V_c\right) C_v \tag{4}$$

where $V_p$ is the electrostatic potential of holes within the PEDOT phase, $\mu_p$ is the chemical potential, and $C_v$ is the volumetric capacitance (mol (m$^{-3}$ V$^{-1}$)). It should be noted that the charging of the PEDOT phase is assumed to occur through the formation of an electrostatic double layer, resulting in a volumetric capacitance. The resulting effective potential for hole transport is $V_{\text{eff}} = V_p + \mu_p/e$.

Assuming a Gaussian density of states in the PEDOT:[22]

$$\mu_p = k_B T \ln(p) + eB \tag{5}$$

for $k_B$, $T$ and $e$ being Boltzmann constant, temperature and elementary charge, respectively. $B$ is taken as ~0.77 V as fitted for PEDOT:PSS in our previous work,[22] along with a concentration dependent hole diffusivity $D_p$, given in eqn (6) for $p$ in mol m$^{-3}$:

$$D_p = 2.3 \times 10^{-5}\ \text{m}^2\ \text{s}^{-1}\left(0.93 - \frac{1.1}{1 + \exp\left(\frac{(p - 71)}{23}\right)}\right) \tag{6}$$

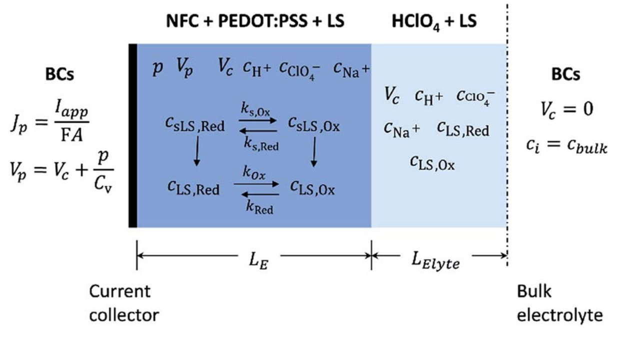

Fig. 2 Geometry of the model system with the various species and quantities listed in addition to the prevailing redox and dissolution reactions, for each region of the device. The applicable boundary conditions (BCs) at the contact and bulk electrolyte are also defined. Solid LS species sLS,Red & sLS,Ox are uncharged, while they dissolve into negatively charged LS,Red & LS,Ox and $Na^+$.

When LS is incorporated in the electrode preparation as described in the Experimental section, the dissolution of solid LS from the electrode domain and its subsequent release into the bulk electrolyte must be accounted for in the model. The dissolution of solid LS (oxidized and reduced forms) is described by eqn (7):[23]

$$r = -k_{\mathrm{r}}(c_{\mathrm{sat}} - c_{\mathrm{LS}});\ (c_{\mathrm{sat}} - c_{\mathrm{LS}}) \geq 0 \tag{7}$$

where $k_{\mathrm{r}}$ is a material and morphology specific dissolution rate constant and $c_{\mathrm{sat}}$ is the saturation concentration, here set to 0.35 M, given a solubility limit of 150 g $\mathrm{L}^{-1}$ of LS in the free electrolyte. Sodium counter-ions to the negatively charged dissolved LS species (see Fig. 2) are also generated in the dissolution process at the same rate.

Given the quinone reduction mechanism in acidic media detailed in earlier studies,[24] the redox reaction rate of LS (solid or dissolved) is described by the concentration dependent Butler–Volmer type kinetics in eqn (8):[25]

$$r = k_{\mathrm{Ox}}c_{\mathrm{Ox}}c_{\mathrm{H^+}}\exp(\alpha_{\mathrm{Ox}}f\eta) - k_{\mathrm{Red}}{c_{\mathrm{Red}}}^2\exp(\alpha_{\mathrm{Red}}f\eta) \tag{8}$$

$$\eta = \left(V_{\mathrm{p}} + \frac{\mu_{\mathrm{p}}}{e}\right) - V_{\mathrm{c}} - E \tag{9}$$

$$E = E^0 - \frac{2.303}{f}\mathrm{pH} \tag{10}$$

where $\alpha_{\mathrm{Ox}}$ and $\alpha_{\mathrm{Red}}$ are the transfer coefficients for oxidation and reduction reactions, with reaction rate constants $k_{\mathrm{Ox}}$ and $k_{\mathrm{Red}}$ respectively. The overpotential $\eta$ is defined in eqn (9), where the Nernst equilibrium potential $E$ of the quinone redox in LS is dependent on its standard redox potential $E^0$ and the local pH[26] (eqn (10)). The resulting generation/consumption rates of; LS species, hydrogen protons and electrons (holes in the PEDOT), due to the redox reaction, scale with the rate defined in eqn (8) and the stoichiometry of the overall reaction shown in Fig. 1 (and in ESI†).

In implementing the model as described by the eqn (1)–(10), the following assumptions and initial conditions were made:

(i) The modelled electrodes are homogeneous in the initial distribution of species and morphology, with assigned single effective diffusivities for $D_{c_i}$ in the electrode domain (see ESI†).

(ii) $k_{\mathrm{r}}$ is considered being constant, with an estimated value obtained by fitting to experimental leakage tests (see ESI† and later discussions).

(iii) $C_{\mathrm{v}}$ (in mol ($\mathrm{m}^{-3}$ $\mathrm{V}^{-1}$)) is calculated from a specific capacitance of 21 F $\mathrm{g}^{-1}$, which was obtained from cyclic voltammetry in our previous article.[10]

(iv) A steady state solution at zero applied voltage was used as the initial condition for all transient simulations. When LS is involved, the redox reactions are turned off for this initial condition since $E^0 = 0.52$ V is far away from the applied 0 V.[10]

(v) The influence of cycling-induced (electro)chemical instability of LS is not considered.

### PEDOT:PSS + NFC electrodes

We establish consistency in our modelling by first capturing the double-layer capacitance that ensues in a PEDOT:LS 1_0 electrode, thereby decoupling the influence of LS. Given that $D_{c_i}$ for the supporting electrolyte ions $\mathrm{ClO_4}^-$ and $\mathrm{H}^+$ in the bulk electrolyte, can be obtained from previous experimental studies,[27] the effective $D_{c_i}$ for these ions in the electrode domain can be obtained by fitting the experimental charge–discharge data as show in Fig. 3a. The good fit to the experimental data shows that the model can reproduce the ohmic potential drop during discharge, seen in the inset of Fig. 3a.

By applying these obtained parameters, we further deduce the redox behaviour of the free LS species in the electrode by matching the experimental charge–discharge data for a similar PEDOT:LS 1_0 electrode but with 50 g $\mathrm{L}^{-1}$ of LS added to the bulk electrolyte (Fig. 3b). This provides the redox transfer coefficients ($\alpha_{\mathrm{LS,Ox}}$ and $\alpha_{\mathrm{LS,Red}}$) and reaction rate constants ($k_{\mathrm{LS,Ox}}$ and $k_{\mathrm{LS,Red}}$) for dissolved LS. Fig. 3b shows a comparison of the model with experimental data for the first cycle; thereafter, the capacity increases with cycling as more LS is transported into the electrode, see Fig. 3c (given an initial state without LS loading at the electrode preparation). This diffusive transport is dictated by the

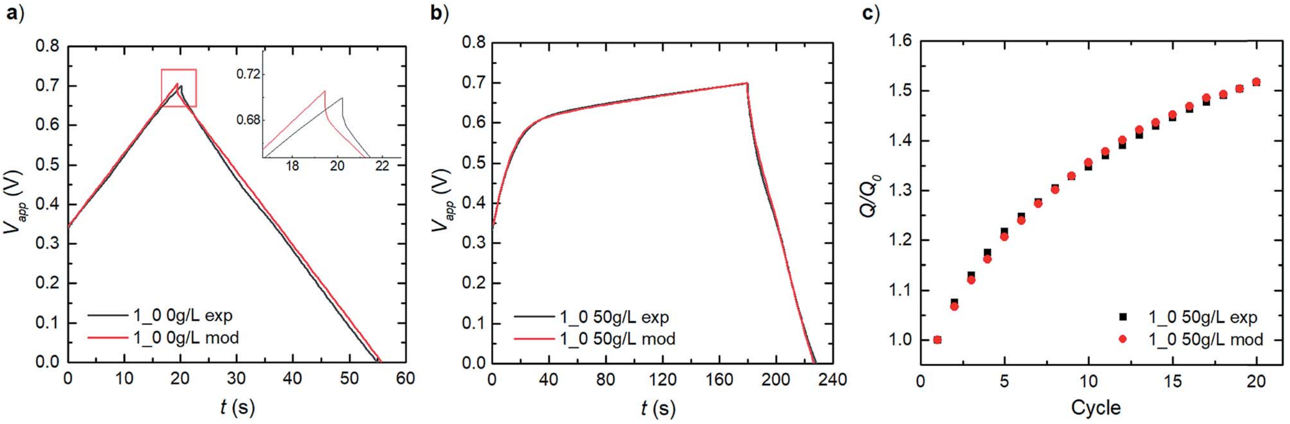

Fig. 3 Comparison of model and experimental results for galvanostatic charge–discharge at 566 μA (2 A $\mathrm{g}^{-1}$): (a) PEDOT:PSS + NFC without preloaded LS (1_0) and 0 g $\mathrm{L}^{-1}$ LS in electrolyte (no changes with cycling). (b) Cycle 1 of 1_0 electrode with initial 50 g $\mathrm{L}^{-1}$ LS dissolved in bulk electrolyte. (c) Relative discharge capacity recorded for 20 cycles following (b). $L_{\mathrm{E}}$ is 52 μm in both (a) and (b).

diffusivities of LS species in both the electrolyte and the electrode domains. Given that $D_{\mathrm{LS,Red}}$ in the electrolyte can be obtained from a previous study,[28] we adopted the same value for its reduced form ($D_{\mathrm{LS,Ox}}$) herein. Then, their effective values within the electrode domain can be estimated *via* fitting to experimental relative discharge capacity data (Fig. 3c).

## PEDOT:PSS + NFC + LS electrodes

For PEDOT:LS 1_2 electrodes, *i.e.* with LS loaded during preparation, the charging response includes contributions from both solid and dissolved LS species (Fig. 4a). To avoid numerical artefacts and for a consistent transient solution, we select the second experimental cycle as our cycle 1 herein. This also helps estimate the initial concentrations of both solid and dissolved LS in all cases (Fig. S1†), by varying both while targeting the best-fit with experimental data, after the initial LS mass at electrode preparation is discounted by first cycle coulombic efficiency. Given that the effective diffusivity of solid LS species is negligible compared to that of the dissolved LS species in the electrode, the solid LS redox ($c_{\mathrm{sLS,Red}} \leftrightarrow c_{\mathrm{sLS,Ox}}$) contributes minimally to the capacity compared to the dissolved LS redox ($c_{\mathrm{LS,Red}} \leftrightarrow c_{\mathrm{LS,Ox}}$). This is also reflected in the model with their respective reaction rate constants (see eqn (8)). The rate constants for dissolved LS species are orders of magnitude greater than for the solid LS, which is expected since – in reality, only the outermost surface of a static lump of solid LS contacts the electrolyte. As cycling continues, relative discharge capacity decreases with time as solid LS dissolves and simultaneously diffuses out into the electrolyte (Fig. 4b). We verified that this capacity decay is primarily dissolution/diffusion driven, by comparing the capacity decay with another experiment where the electrode is cycled only twice, then left to rest for 20 minutes before continuing cycling (see Fig. S2†).

As described in our previous work, the relative discharge capacity of the electrode can be stabilized by the addition of LS to the electrolyte.[10] The model reproduces the trends in relative discharge capacity for 20 cycles of 1_2 0 g L$^{-1}$ LS, 1_2 50 g L$^{-1}$ and 1_2 100 g L$^{-1}$ (Fig. 4b). For 1_2 0 g L$^{-1}$, Fig. 4c shows the corresponding evolution of the galvanostatic charge–discharge response with cycle number. Note that the higher charging voltage plateau (at ~0.6 V) from $c_{\mathrm{sLS,Red}} \leftrightarrow c_{\mathrm{sLS,Ox}}$ fades as the cycle number increases, since LS gradually dissolves and diffuse out of the electrode over time. Hence, a transition from a *battery-like* to a *supercapacitor-like* behaviour is observed for the system. Fig. S3† presents the respective charge–discharge responses for both 1_2 50 g L$^{-1}$ and 1_2 100 g L$^{-1}$. The concentration profiles for fixed and dissolved LS within the electrodes after 20 cycles are shown in Fig. 4d. The addition of LS to the electrolyte decrease the diffusional leakage out from

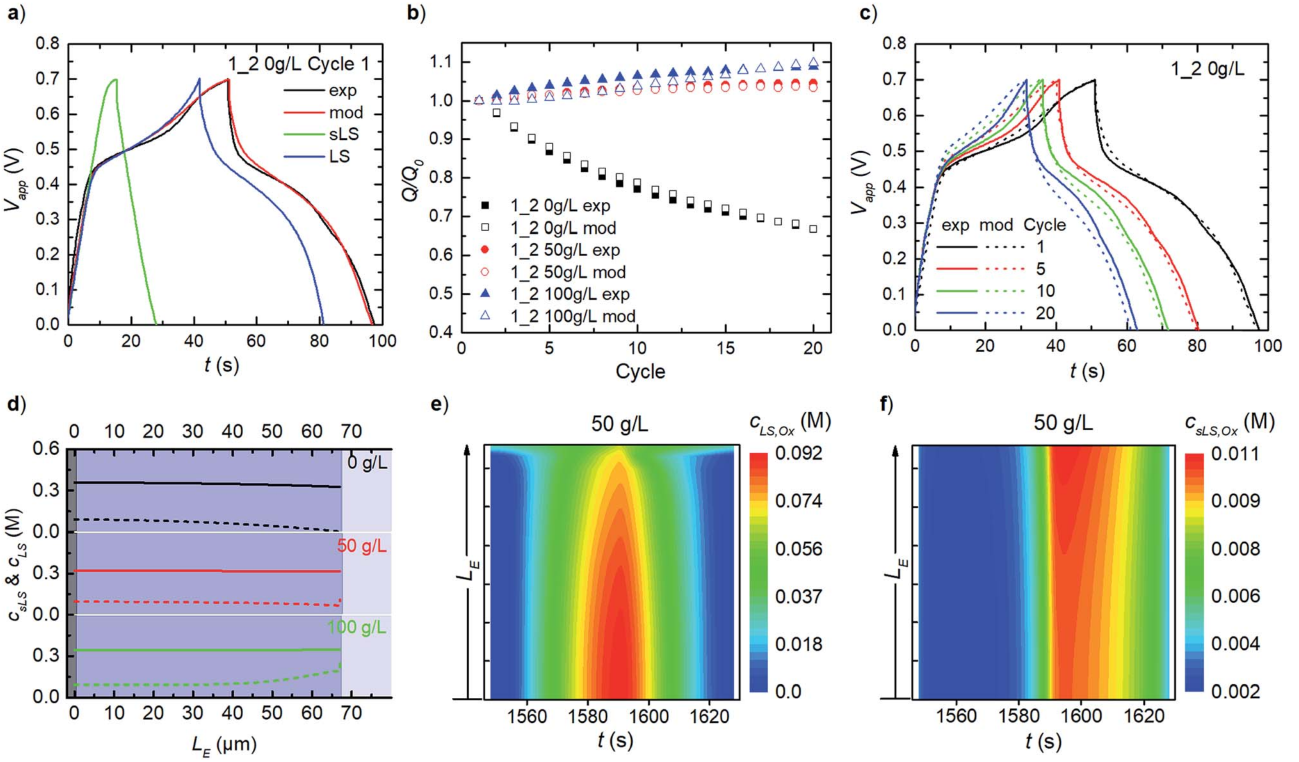

Fig. 4 Model (mod) and experimental (exp) results for galvanostatic charge–discharge at 1689 μA (2 A g$^{-1}$), using electrodes initially loaded with LS (1_2): (a) cycle 1 of 1_2 without LS added in bulk electrolyte. Modelled contributions of both solid (sLS) and dissolved (LS) species to capacitance are shown. (b) Relative discharge capacity – normalized to first cycle ($Q/Q_0$) for 20 cycles of 1_2 with/without added LS in the electrolyte. (c) Transient behaviour during cycling for 1_2 0 g L$^{-1}$. (d) Calculated concentration profiles of total solid LS species (sLS,Red + sLS,Ox, solid line) and total dissolved LS (LS,Red + LS,Ox, dashed line) in electrode thickness $L_E$, at end of cycling. (e) and (f) Calculated time-varying heat maps of LS,Ox and sLS,Ox, respectively, during cycle 20.

the electrode, thereby maintaining a higher concentration of dissolved LS within the electrode. This in turn slows down the dissolution of solid LS (see eqn (7)). The stabilization of discharge capacity is thus caused by maintaining/increasing both dissolved and solid LS within the electrode. The relative increase in discharge capacity for 50 g $L^{-1}$ in Fig. 4b can be explained by the dissolution of solid LS into the more reactive dissolved LS within the electrode. For 100 g $L^{-1}$ LS, the concentration is high enough for LS to diffuse in from the electrolyte into the electrode.

As concentrations and mass transport vary throughout the electrode, it is of interest to analyse the spatial distribution of the redox reactions in the model. Time-varying heat maps of $c_{\mathrm{LS,Ox}}$ and $c_{\mathrm{sLS,Ox}}$ in the electrode domain during cycle 20 for 1_2 50 g $L^{-1}$ are shown in Fig. 4e and f. The oxidation of dissolved LS occurs throughout the whole electrode, with the highest concentrations of oxidized LS found close to the contact, reflecting the concentration profile of dissolved LS (Fig. 4e). At the electrode–electrolyte interface, oxidized LS is present during the whole cycle as a result of diffusional exchange with the electrolyte. For solid LS (Fig. 4f), the highest concentration of oxidized species is found close to the electrolyte interface. Since the electronic transport is faster than the ionic transport within the electrode, this behaviour is expected as the ionic transport causes ohmic losses within the electrode. Note that the solid oxidized LS concentration is substantially lower than the dissolved one.

In the previous sections we have demonstrated that the model quantitatively captures the major characteristics in galvanostatic charge–discharge cycling. Cyclic voltammetry (CV) is another frequently used method for supercapacitor characterization. In Fig. S4,† the model is compared to previously reported CVs of PEDOT:LS electrodes.[10] The CV is reproduced well for 1_0 electrodes, although some minor side reactions seem to be present, which are not accounted for in the model. For the 1_2 electrode, the CV is reproduced fairly well, but some deviations, especially for the cathodic reaction, are present. This indicates that a more complex reaction model would be needed to reproduce the second cathodic peak in the CV.

## Ideal system behaviour and device design directions

The results and discussion so far have shown the behaviours of the electrode systems during short cycling (20 cycles), with the model being capable of reproducing transient experimental results. However, reliable electrochemical energy storage systems are expected to be able to undergo several thousand charge–discharge–rest cycles within their lifetime.[29] Therefore, Fig. 5a shows the expected charge–discharge response of the three scenarios from Fig. 4b at steady operation by cycling the steady state concentration profile results for the same three electrode testing setup. We calculate from our model that the three cases (1_2 0 g $L^{-1}$, 1_2 50 g $L^{-1}$ and 1_2 100 g $L^{-1}$) reach this steady state at 2, 5 and 44 hours respectively. It was observed in Fig. 4b that the relative discharge capacity increases within 20 cycles for both the 1_2 50 g $L^{-1}$ and 1_2 100 g $L^{-1}$ electrodes. At steady state, the discharge capacity has increased even further for the 1_2 100 g $L^{-1}$ electrode. Interestingly, for the 1_2 50 g $L^{-1}$ electrode the discharge capacity instead decreases from cycle 20 to steady state. The initial increase can be understood by considering the dissolution of solid LS, which temporarily increases the concentration of dissolved LS within the electrode.

Based on the developed model, we explore two ideal cases; when the LS is confined in the electrode domain as either only solid, or only dissolved forms – without release to the bulk electrolyte (Fig. 5b). The solid LS case can be achieved by making LS insoluble in the solvent/electrolyte, and the dissolved case can be derived when a perfect separator or a capping membrane suppresses the electrode domain from releasing LS into the bulk electrolyte. From the galvanostatic charge–discharge curves it is evident that the case with dissolved LS is superior and provides the highest capacity and discharging voltage. Thus, the model indicates that the best performance of the PEDOT:PSS + NFC + LS electrodes will be obtained by using a good solvent for LS and coatings which encapsulate the electrodes to prevent leakage of LS out from the electrodes.

Furthermore, we proceed to simulate the steady-state operation of hypothetical half-cells assembled of both 1_0 and 1_2

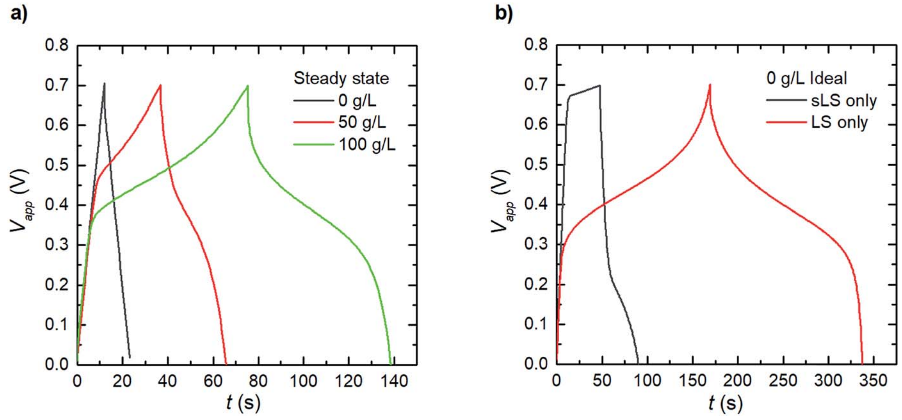

Fig. 5 Simulated electrode response under galvanostatic charge–discharge at 1689 μA (2 A $g^{-1}$) for 1_2 electrodes. (a) At steady operation (after long cycling), and (b) for idealized cases where LS is confined in electrode domain in only solid (sLS) or dissolved (LS) form.

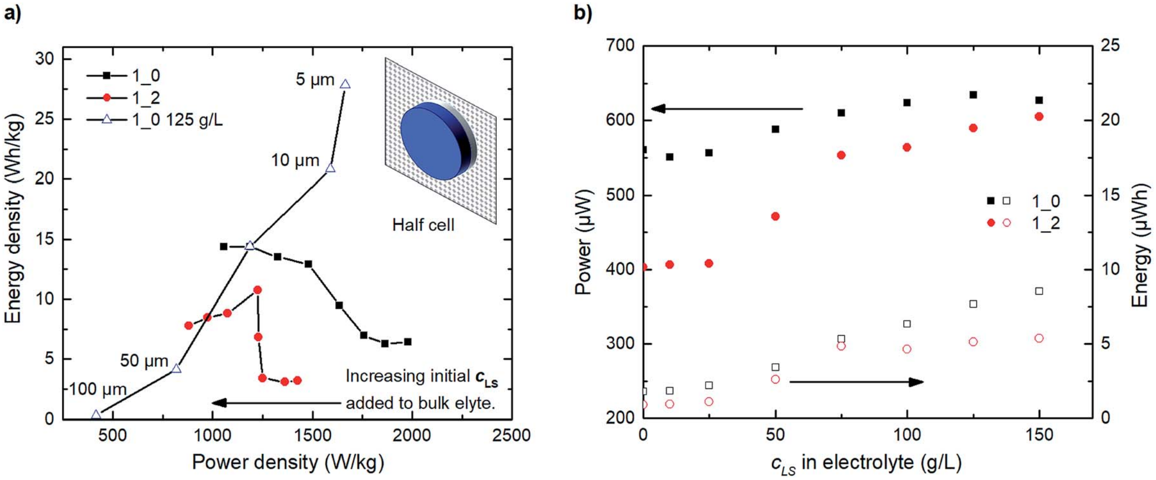

Fig. 6 Simulations of steady state operation of a hypothetical half-cell. (a) Ragone plots from simulated discharge response at steady operation (charge–discharge at 1689 μA) for 0, 10, 25, 50, 75, 100, 125 and 150 g $L^{-1}$ LS in the electrolyte. Nominal electrolyte thickness is 30 μm for 1_0 and 1_2. LS species are confined within the half-cell. The Ragone plot is normalized by the total active species mass (PEDOT + LS). (b) Calculated discharge power and energy for a half-cell made with either 1_0 or 1_2 electrodes.

electrodes (electrodes and 30 μm electrolyte). This investigation emphasizes the compromise between energy and power with increasing initial LS added to the bulk electrolyte. The Ragone plot in Fig. 6a shows that, as the amount of added initial LS to the bulk electrolyte increases, we sacrifice some power density to improve energy density. The trend for the 1_0 electrode is monotone; the more LS the lower power density and the higher energy density. For the 1_2 electrode the trend is more complex with an energy density maximum occurring around 75 g $L^{-1}$ LS in the electrolyte. The decrease in energy density after the maximum is related to increasing amount of low-contributing solid LS within the electrode. The charge–discharge profiles used to construct Fig. 6a and b can be seen in Fig. S5.† We also studied the influence of the electrolyte thickness in the half-cell for the 1_0 125 g $L^{-1}$ LS configuration. Both energy and power density decrease with thickness, as LS far out in the electrolyte is inaccessible to the electrode. One should keep in mind that these results are valid for the steady-state operation. For short term usage and operation, it can still be beneficial to preload LS within the electrodes. Also, preloading of LS can be a convenient way of setting the final concentration of dissolved LS within a closed cell configuration from a production point of view.

Fig. 6b shows that small amounts of initially added LS in the bulk electrolyte (<50 g $L^{-1}$) appear to be inadequate to influence power or energy to a large extent, therefore leading to initially stable power and energy densities, see Fig. 6a. At concentrations greater than 50 g $L^{-1}$, LS redox reactions start contributing significantly to the overall capacitance, thereby increasing power and energy, until a flat in energy is observed starting at ≈125 g $L^{-1}$. Beyond this optimal point, the amount of initially added LS in the bulk electrolyte becomes excessive and adversely affects the coulombic efficiency, in which case not all oxidized dissolved LS during charging can be returned to their previous reduced forms after discharge.

## Conclusions

A novel modelling approach to describe the power and energy densities of CP redox-enhanced supercapacitors has been developed based on the Nernst–Planck–Poisson equations and concentration-dependent Butler–Volmer type kinetics. The model reproduces a wide range of experimental data including transient device trends. A major benefit of the model over the commonly employed equivalent circuit models is that each introduced quantity has a well-defined physical denotation. The model can also capture complex coupled nonlinear processes such as dissolution/release of active species, a necessity to model these complex supercapacitor systems adequately. Our model provides several fundamental insights on the connection between device performance and transport processes within the supercapacitors. The model is further used to suggest a direction for optimal design based on the extracted parameters from experimental data. Although the model accounts for the major processes within the studied redox-enhanced supercapacitors, it can still be further refined. The current model assumes homogeneous electrodes, neglecting microscopic or macroscopic inhomogeneities. By incorporating such aspects, in combination with detailed morphological studies of the electrodes, the description of the mass transport can be further improved. Also, as indicated by the CVs, the current reaction model needs to be refined to capture side reactions and more details of the LS redox reactions. Altogether, this work demonstrate how complex CP-based supercapacitors can be analysed at high detail far beyond what can be achieved using equivalent circuit models, thereby providing additional insights and tools for further development of the field.

## Conflicts of interest

A spin-out company, LIGNA Energy AB, has recently been established that aims at commercializing electrical energy storage technology in part based on forest-based biopolymers. The results from this work may be of importance for the work and development of that company. LIGNA Energy is in part owned by Linköping University (LiU Invest), RISE and researchers (*e.g.* Isak Engquist, Magnus Berggren, Jesper Edberg) of LiU and RISE.

## Acknowledgements

This work was financially supported by the Knut and Alice Wallenberg foundation, Linköping University and industry through the Wallenberg Wood Science Center and Wallenberg Scholar, the Swedish Government Strategic Research Area in Materials Science on Advanced Functional Materials at Linköping University (Faculty Grant SFO-Mat-LiU No. 2009-00971), and the Swedish Foundation for Strategic Research.

## References

1 M. M. Pérez-Madrigal, M. G. Edo and C. Alemán, *Green Chem.*, 2016, **18**, 5930–5956.
2 I. Shown, A. Ganguly, L.-C. Chen and K.-H. Chen, *Energy Sci. Eng.*, 2015, **3**, 2–26.
3 D. P. Dubal, S. H. Lee, J. G. Kim, W. B. Kim and C. D. Lokhande, *J. Mater. Chem.*, 2012, **22**, 3044–3052.
4 T. C. Girija and M. V. Sangaranarayanan, *Synth. Met.*, 2006, **156**, 244–250.
5 A. Elschner, *PEDOT: principles and applications of an intrinsically conductive polymer*, CRC Press, Boca Raton, FL, 2011.
6 F. N. Ajjan, N. Casado, T. Rębiś, A. Elfwing, N. Solin, D. Mecerreyes and O. Inganäs, *J. Mater. Chem. A*, 2016, **4**, 1838–1847.
7 G. Milczarek and O. Inganäs, *Science*, 2012, **335**, 1468–1471.
8 J. Edberg, R. Brooke, H. Granberg, I. Engquist and M. Berggren, *Adv. Sustainable Syst.*, 2019, 1900050.
9 A. Malti, J. Edberg, H. Granberg, Z. U. Khan, J. W. Andreasen, X. Liu, D. Zhao, H. Zhang, Y. Yao, J. W. Brill, I. Engquist, M. Fahlman, L. Wågberg, X. Crispin and M. Berggren, *Adv. Sci.*, 2016, **3**, 1500305.
10 J. Edberg, O. Inganäs, I. Engquist and M. Berggren, *J. Mater. Chem. A*, 2018, **6**, 145–152.
11 K. Ma, C. Zhang, C. E. Woodward and X. Wang, *Electrochim. Acta*, 2018, **289**, 29–38.
12 F. Barzegar, L. Zhang, A. Bello, N. Manyala and X. Xia, *J. Mater. Chem. A*, 2018, **6**, 17481–17487.
13 H. M. Fellows, M. Forghani, O. Crosnier and S. W. Donne, *J. Power Sources*, 2019, **417**, 193–206.
14 S. W. Feldberg, *J. Am. Chem. Soc.*, 1984, **106**, 4671–4674.
15 T. W. Yeu, K. M. Yin, J. Carbajal and R. E. White, *J. Electrochem. Soc.*, 1991, **138**, 2869–2877.
16 T. W. Yeu, T. V. Nguyen and R. E. White, *J. Electrochem. Soc.*, 1988, **135**, 1971–1976.
17 X. Z. Wang, B. Shapiro and E. Smela, *J. Phys. Chem. C*, 2009, **113**, 382–401.
18 M. Modestov, V. Bychkov, D. Valiev and M. Marklund, *J. Phys. Chem. C*, 2011, **115**, 21915–21926.
19 V. N. Prigodin, F. C. Hsu, J. H. Park, O. Waldmann and A. J. Epstein, *Phys. Rev. B: Condens. Matter Mater. Phys.*, 2008, **78**, 035203.
20 J. Rivnay, P. Leleux, M. Ferro, M. Sessolo, A. Williamson, D. A. Koutsouras, D. Khodagholy, M. Ramuz, X. Strakosas, R. M. Owens, C. Benar, J.-M. Badier, C. Bernard and G. G. Malliaras, *Sci. Adv.*, 2015, **1**, e1400251.
21 A. V. Volkov, K. Wijeratne, E. Mitraka, U. Ail, D. Zhao, K. Tybrandt, J. W. Andreasen, M. Berggren, X. Crispin and I. V. Zozoulenko, *Adv. Funct. Mater.*, 2017, **27**, 1700329.
22 K. Tybrandt, I. V. Zozoulenko and M. Berggren, *Sci. Adv.*, 2017, **3**, eaao3659.
23 J. Siepmann and F. Siepmann, *Int. J. Pharm.*, 2013, **453**, 12–24.
24 P. S. Guin, S. Das and P. C. Mandal, *Int. J. Electrochem.*, 2011, **2011**, 22.
25 M. Nandanwar and S. Kumar, *J. Power Sources*, 2019, **412**, 536–544.
26 T. Rębiś and G. Milczarek, *Electrochim. Acta*, 2016, **204**, 108–117.
27 R. K. Malhotra and L. A. Woolf, *J. Solution Chem.*, 1993, **22**, 351–360.
28 A.-K. Kontturi and K. Kontturi, *J. Colloid Interface Sci.*, 1987, **120**, 256–262.
29 M. O. Bamgbopa, S. Almheiri and H. Sun, *Renewable Sustainable Energy Rev.*, 2017, **70**, 506–518.